Bachelor's Thesis - Division of Synchrotron Radiation Research, Department of Physics

Growth and Electronic Structure of Ultrathin Iron Terephthalate Metal Organic Frameworks

Author:
Mulham Shaikh

Supervisor:
Joachim Schnadt

Project Duration:
2 months

Co-Supervisor:
Rosemary Jones

LUND UNIVERSITY

FACULTY OF SCIENCE

June 2024

Abstract

Metal-organic frameworks (MOFs) are a special class of porous materials highly relevant for their wide range of applications in drug delivery, catalysis, gas sensing and transport, and electrochemical storage devices. Due to their unparalleled flexibility in design and highly tunable parameters, over 90,000 MOFs have been synthesized. Iron-based MOFs in particular are of special interest due to their abundance and low toxicity. MOFs are generally synthesized in bulk or powders but ultrathin MOF films allow for the integration of the material with microdevices. In this thesis, a combination of Atomic Layer Deposition (ALD) and Molecular Layer Deposition (MLD) was used to grow ultrathin films of iron terephthalate MOFs on a rutile $TiO_2(110)$ surface using $FeCl_3$ and terephthalic acid precursors. The interaction and deposition of the precursors were investigated by in situ Ambient Pressure X-ray Photoelectron Spectroscopy (APXPS) at the APXPS endstation on the SPECIES beamline of the MAX IV Laboratory. There is an indication that amorphous Fe-TP MOFs were synthesized to a limited capacity but there was not enough deposition to attenuate the rutile $TiO_2(110)$. The material and deposition should be investigated further with ex-situ methods.

Contents

1 Introduction

There is a special interest in crystalline organic-inorganic hybrid materials, also known as Metal-Organic Frameworks (MOF), for their broad range of applications and far-reaching technological advancements (*1–4*). They comprise metal ion nodes that bind multi-directional organic molecules as "linkers" in the metal-organic network structure. The materials' resulting porous cage-like structures and high surface area can be exploited for catalysis, gas storage and separation, and liquid purification (*1–3*). They have also been shown to be promising materials for drug delivery, gas sensing, and electrochemical energy storage devices (*4*, *5*). Through control of architecture and the specific metals and ligands used, MOFs offer unprecedented flexibility in network topology, geometry, dimensions, and chemical functionality. Physical parameters such as conductivity, porosity, and stability can be tailor-built for the specific application. Consequently, over 90,000 different MOFs have been synthesized (*6*, *7*).

In the work presented here, ultrathin films of iron/terephthalic acid MOFs are grown using a combination of Atomic Layer Deposition (ALD) and Molecular Layer Deposition (MLD). The electronic properties of the surface and the film are analyzed with in situ Ambient Pressure X-ray Photoelectron Spectroscopy (APXPS). Iron-based MOFs are of special interest due to the high abundance of iron. It is also a non-toxic element and is, thus, viable for antibiotic detection, and catalysis (*2*, *8*). Iron-based MOFs have also been shown to be effective in wastewater treatment (*9*).

Most MOFs are synthesized as powders. These are good for laboratory tests but offer limited scalability. Growing ultrathin films of MOFs allow for the integration of the material with microdevices furthering potential applications in electronics and magnetism (*10*). Inorganic ultrathin films are best grown using ALD. It is a vapor phase technique used to deposit thin films in a controlled manner with atomic-scale precision. ALD has become extremely relevant in recent years due to its outstanding capabilities in growing high-quality ultrathin films on small surfaces at the nanoscale. The need for ultrathin films at this scale is especially relevant in the development of more powerful semiconductors. As such ALD has found its way into several applications, including energy storage, solar energy devices, microelectronics, and catalysis. (*11–13*). MLD is an analog of ALD and allows the deposition of organic ligands. Hence, ultrathin films of MOFs can be grown seamlessly with a combination of ALD and MLD (*14*).

The experiment analyzed and discussed in this paper was designed by my supervisors Dr. Schnadt and Dr. Jones along with the rest of the APXPS team at the MAX IV Laboratory. It was conducted at the APXPS endstation of the SPECIES beamline in Max IV. The beamtime involved recreating results from Tanskanen et al, 2018 (*15*). Throughout the beamtime, multiple samples of silicon dioxide and titanium dioxide were used with different sets of precursors to grow iron terephthalic films. X-ray absorption, X-ray Photoelectron, and time-resolved XP measurements were taken during the beamtime to characterize the interaction of the precursors with each other and the surface. I got to participate throughout the entirety of the beamtime. In this thesis, I have analyzed XPS data for experiments conducted with one of the samples: a rutile TiO_2(110) surface. Through this set of data, the interaction of iron terephthalic precursors, $FeCl_3$ and Benzene-1,4-dicarboxylic acid, also known as terephthalic acid (TPA), with each other and with the rutile TiO_2(110) surface is studied. This choice was based on the fact that this experiment produced the most interesting results compared to the rest of the XPS data collected from this particular beamtime.

2 Background

2.1 Metal Organic Frameworks

As described earlier, MOFs are crystalline organic-inorganic complexes. The metal ions or metal clusters are connected with organic "linker" molecules to produce structures of different geometries in one, two, or three dimensions. They are porous materials with the metal-organic sub-unit arranged in a repeating pattern. These subunits are also known as Secondary Building Units (SBU) and describe common topologies. The choice of linkers and metal clusters is crucial for determining the properties of the MOF including pore geometries. The general principle for the synthesis of MOFs requires the connecting of SBUs with bridging ligands. The use of dicarboxylate ligands as linkers for early MOFs was crucial in developing large stable three-dimensional pores (*1*). After basic synthesis, the MOFs can be further modified with other chemical processes to functionalize the MOF.

While classifying all MOFs is an active research area there are three main families of well-studied MOFs classified based on common synthesis methods and properties. These are zeolitic imidazolate frameworks (ZIFs), carboxylate-based MOFs, and zirconium-based MOFs. The MOF studied in this thesis is a type of carboxylate-based MOF. Carboxylate-based MOFs are synthesized using organic molecules with carboxylate (COO^-) functional groups. Some of the earliest MOFs fundamental to the development of MOF research are the MOF-5 (*1*) and HKUST-1 (*16*). MOF-5 is composed of Zn_4O clusters linked using TPA Molecules. Each cluster has 6 TP molecules bridging the zinc atoms with octahedral geometry around the cluster. This MOF has a large surface area in the order of 3000 m^2g^{-1}. The chemical structure of MOF-5 is depicted in Fig. 2.1.

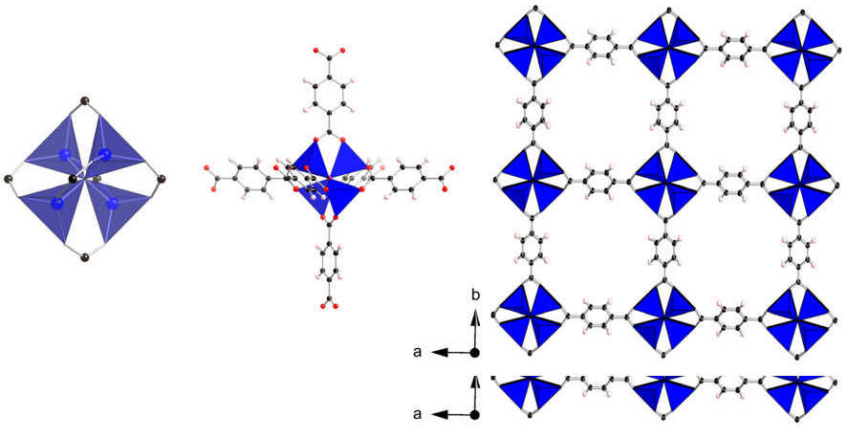

Figure 2.1: Structure of MOF-5. Tetrahedrons represent zinc ions and black spheres represent organic linkers. The middle shows six TP molecules around the Zn_4O cluster. The right shows the 3D network of MOF-5. Image by John Patrick Stephen Mowat, CC BY-SA 3.0 https://creativecommons.org/licenses/by-sa/3.0 , via Wikimedia Commons

The iron-based MOF studied in this thesis also uses a terephthalate (TP) linker provided by a TPA precursor. TP is a common linker for a lot of carboxylate-based MOFs. The molecular structure of TPA and TP are shown in Fig. 2.2. Some known Fe-TP MOFs in bulk form are MIL88-B(*17*) and MIL-53 (*18*). In both the above examples, iron is in the oxidation state of Fe^{+3}. The resulting Fe-TP film grown in the original paper (*15*) shows a mixture of two possible types of bonding structures. These are described in Fig. 2.3.

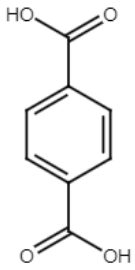

(a) Terephthalic Acid (TPA)

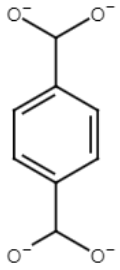

(b) Terephthalate (TP)

Figure 2.2: Structure of TPA and TP

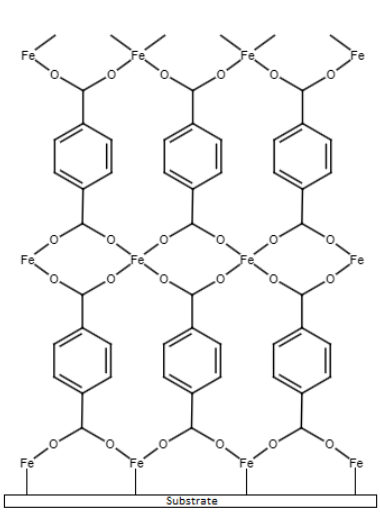

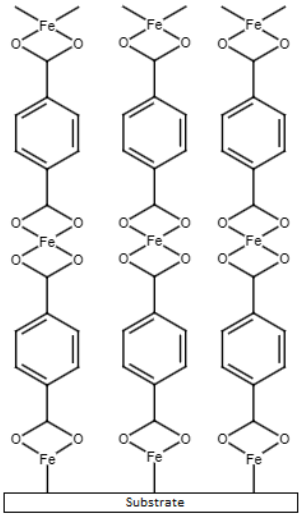

Figure 2.3: The two possible MOF structures for Fe-TP MOF films reproduced from reference (*15*)

2.2 Atomic Layer Deposition and Molecular Layer Deposition

Atomic Layer Deposition (ALD) is a subclass of Chemical Vapor Deposition (CVD) reaction used to grow controlled thin films on different target surfaces. It offers a high degree of control on film thickness, composition, and conformity and has thus become an increasingly important process in research and industry, especially in the semiconductor industry (*11*). ALD and MLD in MOFs have also become an increasingly important research area. For example, there is a lot of interest in using MLD and ALD to functionalize and tune MOFs for improved catalysis (*10*, *19*). As stated previously, there is a strong demand for efficient means of growing ultrathin film of MOFs for microdevice integration.

In a typical ALD process to grow, for example, a transition metal oxide film on the surface of a given sample, the target surface is dosed with precursors sequentially. The sample is dosed with the first precursor, which reacts with the sample surface under optimal pressure and temperature by adsorption. This step for each precursor is known as a half cycle. After a full layer of the precursor is adsorbed, this layer is dosed with the second precursor. By the same process, the second precursor layer is adsorbed on the first precursor. This constitutes the second half cycle. The reaction between the two by ligand exchange forms the required film and is described in Fig. 2.4. A high degree of control over the film thickness is achieved by controlling the number of cycles.

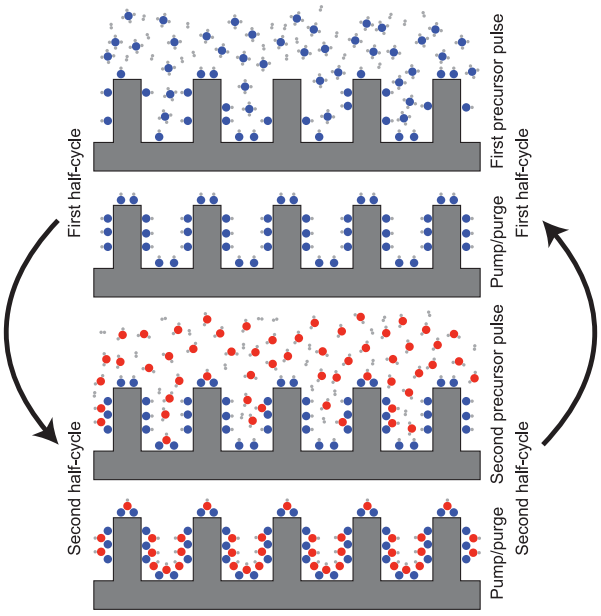

Figure 2.4: ALD process, provided by the courtesy of Dr. Schnadt

ALD is good for depositing metals and inorganic films but it cannot grow organic films. This is where MLD comes in. MLD, like ALD, uses the self-limiting property of the surface to deposit thin layers. The precursors for MLD are also dosed sequentially in cycles. A significant challenge for MLD is finding precursors with sufficient vapor pressure and thermal stability to prevent their breakdown before their chemisorption by the surface. Common precursors for MLD are bifunctional organic molecules to allow for seamless film growth. The combination of ALD and MLD together opens up the opportunity to grow all kinds of organic-inorganic heterostructures,

The dosing of precursors in ALD/MLD in this experiment is done by pulsing the precursors into the reaction cell. Pulsing here means that the precursors are pumped in pulses and each pulse is purged with an inert gas. This purging step also flushes the byproducts of the reaction and remaining precursors out of the cell. To grow films of inorganic-organic complexes, a combination of ALD and MLD can prove to be very effective (*10*). With ALD, a layer of the $FeCl_3$ precursor can be deposited on rutile $TiO_2(110)$ with the iron bonding with lattice oxygen atoms on the surface as shown in Fig. 2.4. Then with MLD, terephthalic acid precursor can be deposited on the iron layer. As described in the figure, the oxygen atoms in the carboxylic ligands would then bond with the iron. In the next half cycle, $FeCl_3$ would bond with the other carboxylic ligand on the TPA molecule. This way the required MOF could be produced. The by-product HCl would get flushed out.

2.3 Theory Behind Photoelectron Spectroscopy

The photoelectron emission can simply be described by the excitation of bound electrons in the solid by the incoming energy of the x-rays. Using Einstein's and Hertz's discovery of the photoelectric effect, photoemission is described by the equation:

$$h\nu = E_B + E_k + \phi, \tag{2.1}$$

where $h\nu$ gives the energy of the incoming photon, E_B is the binding energy of the electron in the core holes with respect to the fermi level, E_k is the kinetic energy of the photoelectron emitted, and ϕ is the work function of the analyzer. The work function is the minimum energy required for an electron to excite to the vacuum level from the valence band of the material. To understand the photon interaction with matter during photoemission, a semi-classical quantum mechanical treatment is needed.

2.3.1 Quantum Mechanical Treatment

Though photoemission occurs in a single step, it can be approximately explained by a three-step model (*20*). According to this model, an electron in a core level first gets excited by an incoming photon resulting in an electron-hole pair with the excited electron in an unoccupied band energy above the Fermi level of the solid. This electron then propagates to the surface, possibly resulting in inelastic scattering and emission of secondary electrons. Finally, it escapes the surface as a plane wave into the vacuum. In the case of XPS. the electron also traverses through the potential landscape of the analyzer. This represents the work function described earlier.

The Hamiltonian of a single electron held in the potential of the solid $\hat{\mathbf{V}}$ in the presence of an external classical electromagnetic field of vector potential $\hat{\mathbf{A}}$ is given by

$$\hat{\mathbf{H}} = \left[\frac{1}{2m}\left(\hat{\mathbf{p}} - \frac{e}{c}\hat{\mathbf{A}}\right)^2 + \hat{\mathbf{V}}\right]. \tag{2.2}$$

Evaluating the Hamiltonian further we get,

$$\hat{\mathbf{H}} = \frac{\hat{\mathbf{p}}^2}{2m} + \hat{\mathbf{V}} - \frac{e}{2mc}\left(\hat{\mathbf{A}}\cdot\hat{\mathbf{p}} + \hat{\mathbf{p}}\cdot\hat{\mathbf{A}}\right) + \frac{e^2}{2mc^2}\hat{\mathbf{A}}^2. \tag{2.3}$$

Taking an arbitrary function that f, the commutator

$$\left[\hat{\mathbf{p}}, \hat{\mathbf{A}}\right] f = -i\hbar\nabla\hat{\mathbf{A}}f + \hat{\mathbf{A}}i\hbar\nabla f$$

Applying product rule,

$$\left[\hat{\mathbf{p}}, \hat{\mathbf{A}}\right] f = i\hbar f(\nabla\cdot\hat{\mathbf{A}}) - i\hbar\hat{\mathbf{A}}\nabla f + i\hbar\hat{\mathbf{A}}\nabla f.$$

Finally, the commutator is given by

$$\left[\hat{\mathbf{p}}, \hat{\mathbf{A}}\right] f = i\hbar f(\nabla\cdot\hat{\mathbf{A}}) \tag{2.4}$$

Since the wavelengths are larger than bond lengths, the magnetic potential can be taken as constant and perpendicular to the electron. The classical field assumption holds. Then we can describe the potential field as a Coulumb gauge $\nabla\cdot\hat{\mathbf{A}} = 0$ (*20*). This makes the commutator null. Additionally, in equation 2.3, the quadratic potential term in the Hamiltonian can be neglected. Hence, The total Hamiltonian is then given by:

$$\hat{\mathbf{H}} = \frac{\hat{\mathbf{p}}^2}{2m} + \hat{\mathbf{V}} - \frac{e}{mc}\hat{\mathbf{A}}\cdot\hat{\mathbf{p}}. \tag{2.5}$$

The Hamiltonian can be rewritten as $\hat{\mathbf{H}} = \hat{\mathbf{H}}_0 + \hat{\mathbf{H}}_1$, where $\hat{\mathbf{H}}_0$ is the original Hamiltonian and $\hat{\mathbf{H}}_1$ is a perturbation that describes the photon-matter interaction:

$$\hat{\mathbf{H}}_0 = \frac{\hat{\mathbf{p}}^2}{2m} + \hat{\mathbf{V}}, \tag{2.6}$$

$$\hat{\mathbf{H}}_1 = -\frac{e}{mc}\hat{\mathbf{A}}\cdot\hat{\mathbf{p}}. \tag{2.7}$$

In time-dependent perturbation theory, the transition probability of electrons from initial state i with wave function ψ_i, to the excited final state f with wave function ψ_f due to a perturbation can be calculated using Fermi's Golden Rule (*20*) as:

$$\omega_{if} = \frac{2\pi}{\hbar}|\langle\psi_f|\hat{\mathbf{H}}_1|\psi_i\rangle|^2\delta(E_f - E_i - h\nu) \tag{2.8}$$

where ω_{if} is the transition probability. $\langle\psi_f|\hat{\mathbf{H}}_1|\psi_i\rangle$ is the matrix element for this interaction. The binding energy cannot be calculated directly from this result. But by taking a "frozen orbital" approximation,

it can be shown that the energies calculated would exactly reflect the binding energies of the orbitals (*11*). The frozen orbital approximation neglects the effects of the core hole produced by photoemission, implying that the electronic states of the system do not change from the initial to the final state of the photoelectron. The linewidth of the XPS peaks measured is directly due to the uncertainty in the lifetime of the core-hole.

2.3.2 Information Obtained from XPS

All elements have unique core energy levels. Depending on the chemical environment, the binding energies of these core levels change. XPS measurements give strong insight into the chemical and electronic structure of the sample using peak widths, and peak positions. The peak separations give characteristic information about the elements and the type of chemical bonds present. For in situ XPS measurements of reactions, chemical shifts are extremely important to quantitatively identify the changes in the chemical environment. In the case of samples with unpaired electrons in the core level, multiplet splitting arises and the orbital splitting ratios are reflected in the corresponding relative peak intensities.

Peaks in XPS data can also occur due to a few different processes and are known as satellite peaks. These processes include plasmon excitations, shake-ups, and shake-offs. Plasmons are quantized oscillations of electrons and get excited by traveling photoelectrons. This results in a loss of energy of the electrons measured. As previously stated, it is assumed that electron states do not change due to photoemission. However, after the excitation of a core electron, the energy distribution of electrons does change which can result in the excitation of valence electrons. These excitations are known as shake-ups if the valence electrons remain bound, and shake-offs if the valence electrons escape. A core-hole decay can also occur by the sample emitting Auger electrons which can result in Auger peaks in the XP spectra.

Inelastic scattering events in solid samples result in secondary electron-hole pairs. This contributes to the background in the XP spectra. Using a model based on Beer-Lambert Law, the inelastic mean free path can be calculated:

$$I(z) = I_0^{\frac{-z}{\lambda}}. \tag{2.9}$$

Here λ is the inelastic mean free path and z is in the direction perpendicular to the sample.

3 Experimental Method

3.1 APXPS Endstation

The experiment was done at the APXPS end-station on the SPECIES beamline at MAX IV. The SPECIES beamline is a soft X-ray beamline that uses a monochromator and an undulator providing a photon energy range of 30 to 1500 eV. The schematic of the end station is shown in Fig. 3.1. One can see from the figure that there are three main parts to the setup: a preparation chamber, an analysis chamber, and the spectrometer. The incoming X-ray beamline ends in the analysis chamber. The chemical reactions are done in the Ambient Pressure ALD cell. This cell has a window for the incoming X-rays to perform XPS.

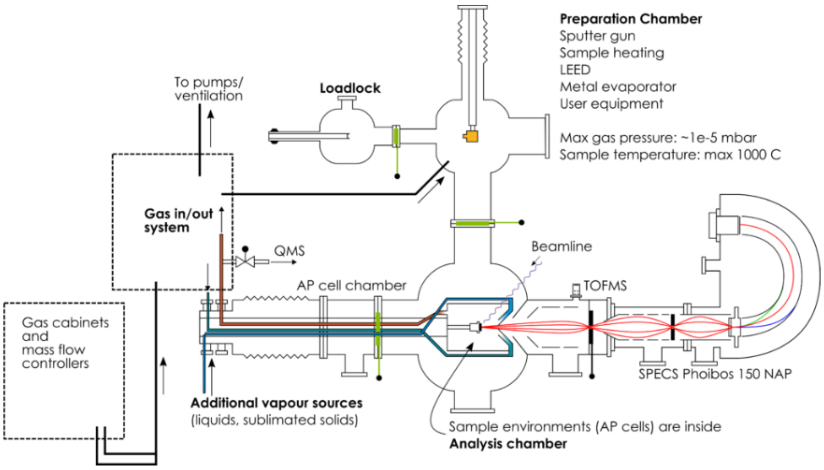

Figure 3.1: Schematic of XPS reproduced by courtesy of Dr. Kokkonen from the SPECIES webpage, https://www.maxiv.lu.se/beamlines-accelerators/beamlines/species/experimental-station/apxps/

Pressure ranges in the system from ultrahigh vacuum to 10^{-5} mbar outside of the cell. The pressure in the AP cell goes up to 20 mbar. However, in this experiment, a maximum pressure of 1 mbar was observed. The sample can be introduced in the preparation chamber. Hereby, it is controlled with a manipulator that allows rotation and movement in all three directions with a controller. The cell itself is held in the cell chamber and then is brought into the analysis chamber. The manipulator is then used to place the sample in the cell.

3.2 XPS Analyzer

A hemispherical electron energy analyzer is used to record the different kinetic energies. This is a pair of conducting hemispherical electrodes at a fixed voltage to bend the trajectories of the electrons. The photoelectrons emitted from the sample are focused by a pair of voltage lenses before entering the electrodes. The electrons with kinetic energy around the "pass energy" of the analyzer follow a circular path with a "pass radius". This represents the center/most trajectory of the electron in the hemispherical analyzer. The lenses retard the incoming electrons around the pass energy. Electrons of a specific kinetic energy are measured by setting voltages for the lens system. The deviations in the trajectory from the pass energy can then be used to measure the kinetic energy. Electrons with energies that are too high or low land on the walls of the electrodes and are not picked up by the detector. The voltages on the lenses change to scan over a range of kinetic energies. The analyzer used here is the SPECS Phoibos 150 NAP.

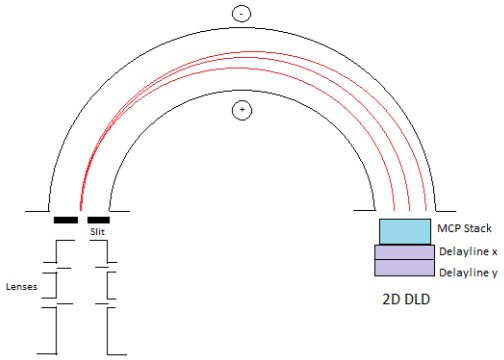

Figure 3.2: Schematic of the hemispherical analyzer

At the end of the hemispherical analyzer, the electrons are detected by a two-dimensional Delayline Detector (DLD). It contains a two-dimensional array of channels that represents kinetic energy on one axis and, depending on the mode, spatial or angular position on the other axis. In this case, the position is not as relevant, hence kinetic energies measured are integrated across the position axis. These measurements can be taken in two different modes: swept and snapshot mode. In snapshot mode, the lens voltages remain fixed, and the entire energy range spans across the detector channels. This is useful for quick measurements, for example, it is used when taking time-resolved measurements during a chemical reaction. However, the different channels are not uniformly sensitive on the multichannel plate. To get rid of the variable sensitivity, swept mode is used when possible. In swept mode, the lens voltages are varied to sweep all the kinetic energies across every detector channel. This makes sure that the entire range of the kinetic energy to be measured is detected by every channel. The energies measured are then integrated and averaged to get rid of the variable sensitivity of the detectors to the incoming electrons. This mode can cover a broader energy range with high energy resolution but takes more time. This is usually done after an ALD cycle (*21*). The data analyzed in this paper are all taken in swept mode.

3.3 Ambient Pressure ALD Cell

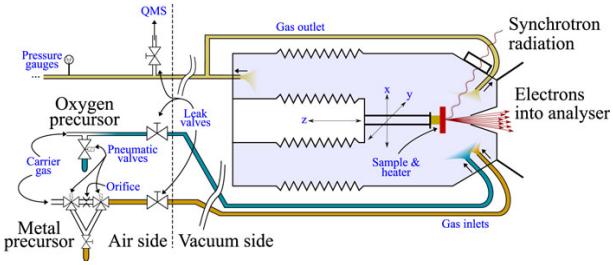

Figure 3.3: Ambient Pressure ALD Cell schematic reproduced from (*21*)

The schematics of the ALD cell are shown in Fig. 3.3. The cell contains two inlet lines directly onto the substrate surface followed by a pumping line outlet. This prevents the mixing of the precursors before making contact with the surface, and the pumped outlet maintains laminar flow across the sample allowing for fast reaction times. An inert carrier gas is used for more effective delivery of the precursors and is also used for purging between half cycles. ALD processes need to be performed at elevated temperatures to prevent condensation of precursors and avoid unreacted precursors remaining in the cell. The temperatures should be high enough to facilitate the reactions but also need to be low enough to prevent the decomposition of the precursors. Temperatures are tuned depending on the film properties required. There is a vacuum heating system placed in the inlets to heat the precursors. A similar heating system is also attached to the walls of the cell near the sample. This also prevents condensation of the precursors on the cell walls. The sample itself is heated using a Pt resistive wire. The ALD cell contains

a thin window for the X-rays to enter through. This window limits the maximum pressure in the cell to 20 mbar whilst keeping the analysis chamber at a high vacuum. As seen in the schematic, the cell contains an aperture to allow high transmission of electrons but reduce the amount of gas entering the analyzer (*21*).

3.4 Sample Preparation

In this experiment, rutile $TiO_2(110)$ was used. The sample's dimensions are 8 x 8 mm and its structure is shown in Fig. 3.4.

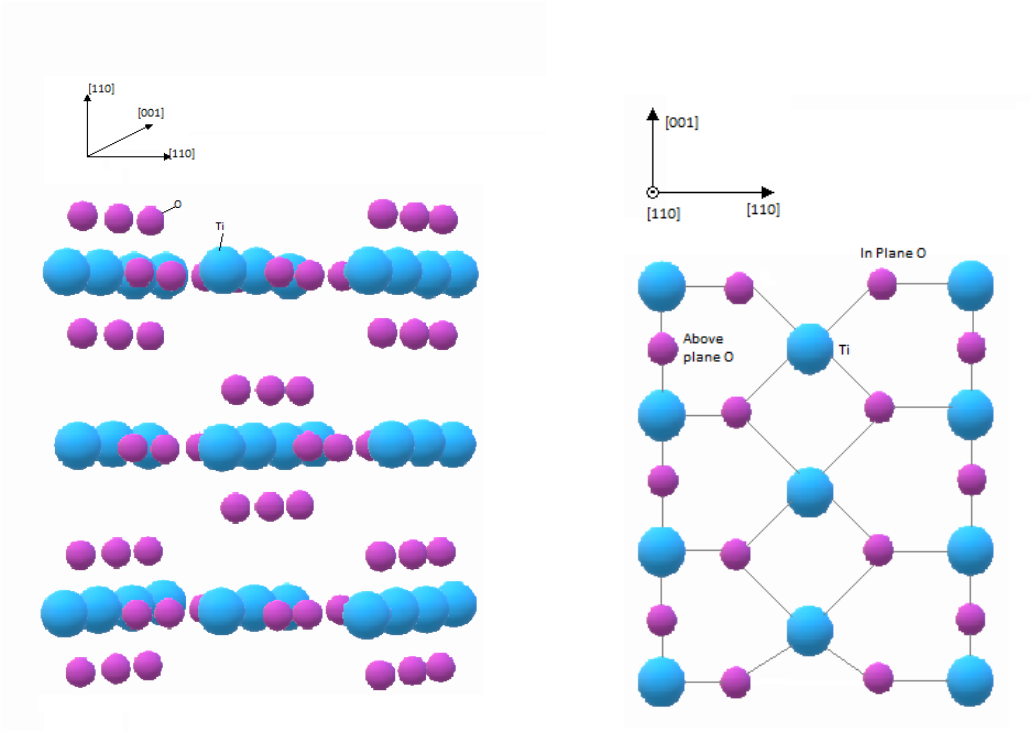

Figure 3.4: Rutile-$TiO_2(110)$ crystal structure on the left and top view of surface on the right.

The sample is prepared by repeatedly sputtering the surface and annealing the crystal in the preparation chamber, see Fig. 3.1. Sputtering cleans the sample by breaking away ions at the surface. The sample is bombarded with a current of ionized particles with energy ranging from hundreds to thousands of eV. The high energy collisions of the incoming particles with the surface atoms result in a collision cascade through the solid. Particles with higher energy than the surface energy leave the solid due to these collisions. This results in the breaking of chemical bonds at the surface and is known as sputtering. Annealing is a process in which a solid's crystal structure is recovered and re-organized by heating. After heating up to the material's annealing temperature, the sample softens, allowing for the ions to relocate by diffusion. Ion impurities deeper inside the crystal diffuse to the surface. This is then followed by recrystallization of the complete solid. Annealing also gets rid of dislocations in the sample and heals the surface of the crystal.

In the preparation chamber, a SPECS argon sputter gun is used. The sample was sputtered with 10^{-5} mbar pressure of ionized argon with a resulting current of 10 mA. The sample was sputtered with a potential of 2 kV for thirty minutes. After sputtering the sample is annealed for ten minutes. The sample was sputtered once again with the same energy and pressure for twenty minutes followed by annealing for another ten minutes. It is important to be careful when sputtering with TiO_2 as oxygen breaks down very efficiently under sputtering. Sputtering hence also damages the TiO_2 surface and should not be done for too long.

3.5 Precursor Dosing

The sample is dosed by pulsing the precursors into the cell as described in Section 2.2. $FeCl_3$ is dosed in the first half cycle and TPA is dosed in the second half cycle. Argon is used as the inert carrier gas. The pulsing is done quite slowly in a time scale of seconds.

The sample and the cell were heated to a temperature of 230 °C. The temperature of the cell and sample were kept constant across all measurements. In Fig, 3.3, the gas tubes are kept at a constant temperature of 150 °C. The precursors $FeCl_3$ and TPA are maintained at a temperature of 150 °C, and 250 °C respectively.

3.6 Data Analysis Methods

3.6.1 Calibration

The kinetic energy measured in the experiment depends on the vacuum level. The vacuum level may not necessarily be constant across the entire surface. The potential landscape of the analyzer also affects the vacuum level. This results in the 'zero' of the energy spectrum shifting away from the Fermi energy level of the material. Additionally, the exact incoming photon energy is not known which can further induce a shift. The work function of the analyzer could be carefully calculated and corrected but this cannot be done without knowing the exact incoming photon energy. Hence, the data measured needs to be corrected to the Fermi level of the sample as it remains constant throughout the material. This way, calibration does not depend on the incoming photon energy or the kinetic energy measured.

In this thesis, the Ti 3p energy level was calibrated to a previously calibrated Ti 3p energy level of a rutile $TiO_2(110)$. The calibration of this peak has been achieved by measuring its Ti 3p level and the Fermi level of an Au foil in good electrical contact with the rutile $TiO_2(110)$ sample.

This calibrated spectrum was taken at an incoming photon energy of 400 eV. The same shift needed to calibrate this spectrum is then used to calibrate C 1s and Cl 2p spectra that were taken at the same incoming photon energy. The calibrated C 1s spectra were then used to correct other C 1s spectra taken with an incoming photon energy of 650 eV. This allowed calibration of the O 1s and Ti 2p spectra; both were taken at an incoming photon energy of 650 eV. O 1s and Fe 2p spectra were measured with photons at 850 eV. These are then calibrated the same way as C 1s. The entire process was then repeated for every other experiment by matching the Ti 2p peaks.

It is worth mentioning that this calibration approach is not entirely reliable as different incoming photon energies look at different depths of the sample. The chemical environment at the surface and in the bulk differ. This could result in small shifts to the peak position that are neglected when matching, for example, O 1s spectra at 650 eV to O 1s spectra at 850 eV. However, given that we do not probe that deeply into the bulk, the changes in the chemical environment are not that different and this approach can still be useful.

3.6.2 Background Removal

In XPS, the kinetic energies of electrons emitted from the sample are recorded. Unscattered emitted electrons do not lose any kinetic energy and correspond to peaks in the spectra. However, due to the sample being a 3D structure, photoelectrons emitted get scattered by the bulk structure and lose their kinetic energy. This contributes to the background in XP spectra. Since most of the scattered electrons lose all their kinetic energy, the background intensity is higher at very low kinetic energies. Hence, the intensity of the background increases with increasing binding energy.

There are three different phenomenological approaches to calculating the background: linear background, Shirley background, and Tougard background (*11*). The linear background removal involves simply subtracting intensities below a line defined by two points. The Shirley method is an iterative approach

that assumes the intensity at a given energy to be proportional to the total intensity at lower binding energies. This assumption holds very well for the way XPS background is generated. The algorithm to calculate the background is given by convergence of the equation:

$$S_n(E) = S_0(E) - k_n \int_{E_{min}}^{E_{max}} S_{n-1}(E')dE' \tag{3.1}$$

In equation 3.1, k_n is given by evaluating $S_0(E_{min}) = 0$. The Tougard background is calculated based on the physics of scattering and processes that give rise to the XPS background. It is a more complicated approach that depends on several precise physical parameters to be reliable. Hence, this approach was not used.

For the experiment data collected and analyzed in this thesis, the linear and Shirley background removal methods were sufficient. For some spectra like oxygen 1s, the intensity before and after a peak does not differ much; the Shirley background is approximately the same as a line background. The line background calculated for the case of oxygen is shown in Fig, 3.5a contrasted with a more detailed Shirley background calculated for Ti 2p in Fig, 3.5b.

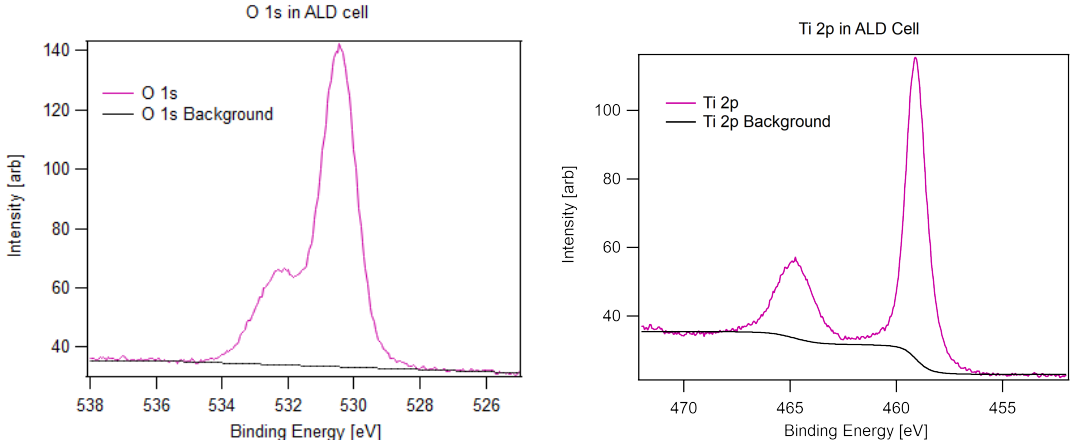

(a) O 1s spectrum with a linear background (b) Ti 2p spectrum with a Shirley background

Figure 3.5: Both the elements' spectra above are taken with the sample in the Cell before any pulsing of precursors.

Additionally, XP spectra collected for Fe 2p do not span the entire range. This makes it difficult and unnecessary to effectively calculate the background. Instead, a constant background was subtracted so that the Fe 2p spectra could be compared to each other.

3.6.3 Peak Fitting

XPS curves often come with multiple overlapping component peaks. The component peaks exist due to chemical and physical processes involving XPS and the chemical reactions occurring. To make quantitative and qualitative analyses, the curves are fit with physically relevant component peaks. The peaks in XPS exhibit both Gaussian and Lorentzian characteristics. Photoelectrons in the core levels get excited by the X-rays to an energy level above the Fermi level. This results in a hole in the core level. Due to the uncertainty principle and lifetime of the core hole, the energy level exhibits a Lorentzian distribution. The Gaussian contribution comes from instrumental errors and phonon broadening. Generally, the Gaussian broadening dominates. This convolution of Gaussian and Lorentzian lines is known as a Voigt profile (*22*).

The peaks above the binding energy of 30 eV correspond to photoelectrons ejected from core levels.

Peaks below the binding energy of 30 eV correspond to photoelectrons emitted from shallow core levels and the valence band. There are also additional peaks in the XP spectra known as satellite peaks. They correspond to photoelectrons emitted due to other physical processes such as Shake-ups, Shake-offs, and Plasmon excitation.

The data analysis as mentioned earlier was done using procedures in Igor Pro 8. A Parameter set of peak position, peak amplitude, Gaussian width, and Lorentzian width are varied by the software to minimize the residuals of the fit. The parameters are constrained to ensure that the fits remain physically relevant. Since the fitting is done after background subtraction, it does not need to be taken into account in the fitting process. Changes in the fitted peak position and widths represent changes in the chemical environment.

After fitting all the different XP spectra separately it was clear that there was not much change in the peak widths and positions after the precursors were pulsed in. As such they were refitted globally linking the peak positions and widths of the specific elements for all spectra taken under the ALD cycles. This involves minimizing residuals simultaneously across all spectra while maintaining the same peak positions and widths.

3.6.4 Uncertainty Analysis

The uncertainty in energy detected depends on Gaussian dispersion due to the energy resolution of the analyzer and the beamline. This is given by the equation

$$\Delta E = \sqrt{\Delta E_{beamline}^2 + E_{analyzer}^2} \tag{3.2}$$

Apart from Gaussian dispersion, the different aspects of data analysis may contribute additional uncertainty. In the work presented here, this is taken as 0.5 eV.

This is not entirely sufficient for uncertainty in peak positions of O 1s and C 1s spectra. Peak fitting for O 1s and C 1s was done based on models for the components. This implies that there may be components not taken into account when fitting. Hence, uncertainty analysis of peak positions is done based on the uncertainty of the fits. This is obtained by fitting with a reasonable initial guess slightly different from the obtained peak positions. The initial guess peak positions except the main peak are held for both O 1s and C 1s spectra. Then the held peaks are varied to stretch out as far as possible while still getting reasonable fits with low residuals. The residuals in general were kept within 10 % of all points along the peaks.

4 Results

After sample preparation, it was brought down into the analysis chamber. Before inserting the sample into the ALD cell, brief XPS measurements were taken with the sample on the manipulator in ultra-high vacuum. The overview of XP spectra across the entire energy range of incoming photon energy of 950 eV was measured. Additionally, C 1s and Fe 2p spectra were measured at incoming photon energies of 400 eV and 850 eV respectively. O 1s and Ti 2p spectra were both collected at 650 eV.

The sample was then swapped over to the ALD cell. A more detailed XPS measurement was taken here with the same incoming photon energies. All the different spectra and their photon energy measurements are displayed in Table 4.1. These remain consistent across all the measurements except Cl 2p. Cl 2p was not measured in the manipulator and additional spectra of Cl 2p at an incoming photon energy of 300 eV were not measured until precursors were pulsed in.

Finally, the two precursors $FeCl_3$ and TPA are pulsed sequentially. XPS measurements are taken after purging half cycle for the first two and a half cycles. The gasses were then pulsed in continuously for twenty complete cycles. XPS measurements were taken again at this point. The last set of XPS measurements were taken after another complete twenty cycles representing a total of forty cycles.

Table 4.1: Different XP spectra measured

Name	**Photon Energy [eV]**	**Pass Energy [eV]**	**Slit**
Overview	950	100	50
Fe 2p	850	50	50
O 1s	850	50	50
O 1s	650	50	50
Ti 2p	650	50	50
C 1s	650	50	50
C 1s	400	50	50
Cl 2p	400	50	50
Cl 2p	300	50	50
Valence Band	300	50	50

All the relevant spectra measured are put together and presented in Fig. 4.1. It is important to note that the Cl 2p spectrum taken at the manipulator in ultra high vacuum is taken from the complete overview spectrum. Additionally, only O 1s and Ti 2p could be calibrated among the data collected in the manipulator. Doubles of C 1s an d O 1s were not taken here so the rest of the spectra taken in the manipulator in ultra high vacuum could not be calibrated. This makes it difficult to rely on absolute peak positions for the manipulator and separation is more relevant to infer chemical shifts. Another key point to note is that the spectra are not normalized to each other. This could have been done using Au foil or manually normalizing using secondary electrons for each spectrum. Consequently, the intensities of different spectra cannot be compared. Instead, ratios of peak intensities and peak fractions can be used to make a similar analysis.

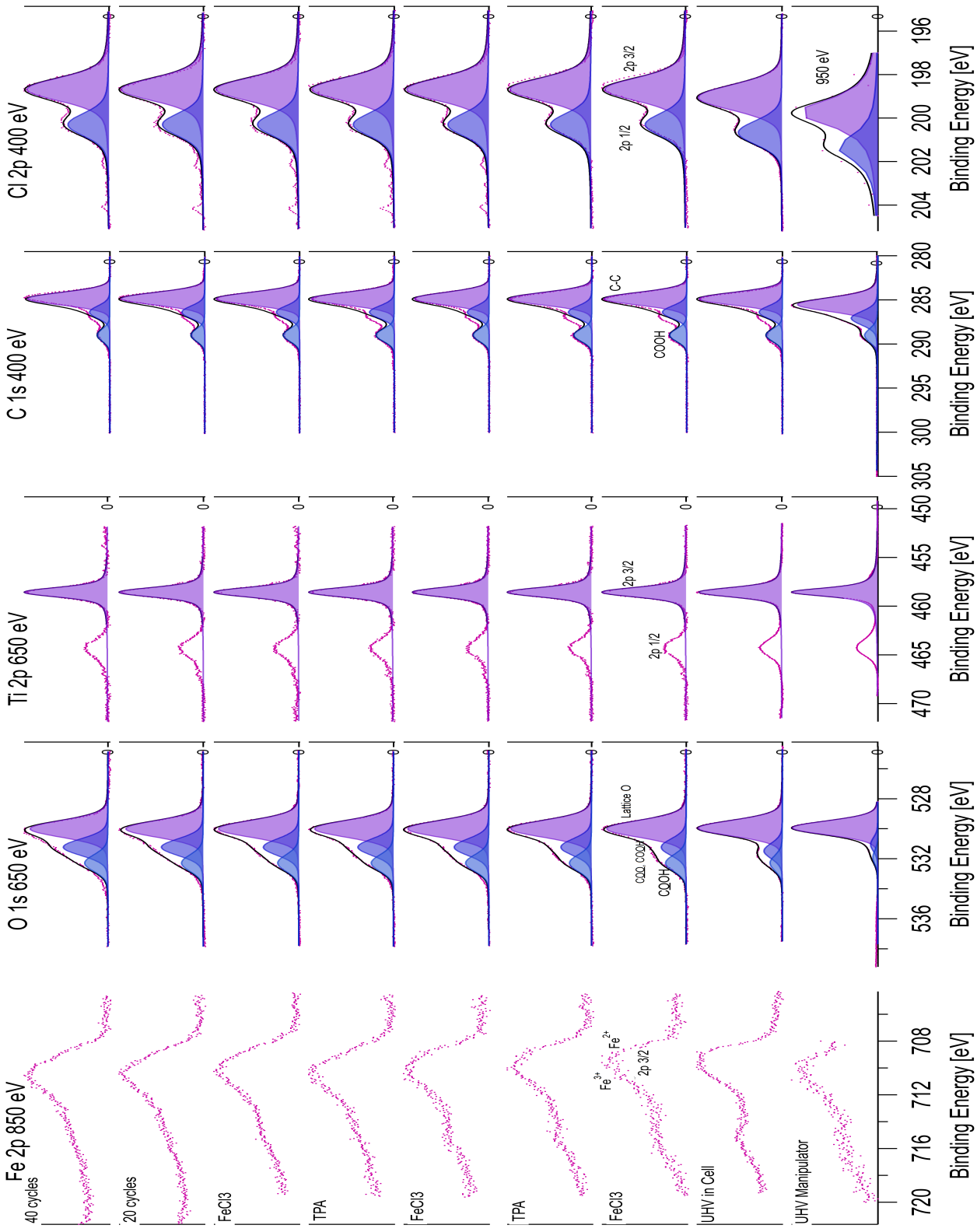

Figure 4.1: XPS data of all elements with relevant component peaks

4.1 O 1s

Looking at the O 1s spectra in Fig. 4.1, three component peaks can be observed. The primary peak at 530.0 eV can be assigned as the main O 1s peak due to the lattice oxygen from TiO_2. This is reflected by the fact that it has the largest peak. It can also be seen that this peak's intensity gets lower with MLD cycles compared to the other oxygen peaks. This further implies that the surface gets partially covered by precursors. The other two peaks are found to be at 531.2 eV and 532.3 eV and correspond to the different oxygen atoms in the carboxylic group of a TPA molecule. In Fig. 2.2a, the double bonded oxygen contributes to the peak at 531.2 eV, and protonated oxygen in the OH group contributes to the peak at 532.3 eV.

Given, that TPA precursors are used to grow Fe-TP MOFs, the component peaks for the fitting are modeled after the work presented by Schnadt et al.(*23*) and Pathey et al.(*24*). In their work, isonicotinic acids and other similar molecules are deposited onto rutile TiO_2(110) and their resulting structures are extensively studied. This is relevant as both isonicotinic acid and TPA have a benzoic acid-like structure. These results also show that the 1s energy level of both the oxygen atoms in a deprotonated carboxylic group is the same as the energy of the double-bonded oxygen in a protonated carboxylic group on rutile TiO_2(110) surface. This is possibly indicative of MOF structures.

Originally, I fitted all O 1s spectra separately with three components but there was no significant change in the peak positions and the full-width half maximums (FWHM) for measurements taken after the precursors were pulsed in. Hence, all O 1s spectra that were taken during MLD cycles were fitted globally with FWHM and peak positions linked in Igor Pro 8. The O 1s spectra taken before dosing were not linked as they have noticeably different shapes and the global fits produced high residuals. Originally they were fit with two components but it can be inferred from element spectra in Fig. 4.1 that there are impurities and deposition on the surface from the beginning of the experiment with the sample in the manipulator. Hence, it is reasonable to assume all three components of the O1s spectrum should be faintly visible with the sample in the analysis chamber and the cell. Hence these were also fitted for three peaks. The final peak positions, FWHMs, and peak separations are described in Table 4.2. The uncertainty for peaks is calculated by varying peak positions in global fits. Uncertainty in peak separation is calculated and obtained using Gaussian propagation.

Table 4.2: O 1s peak positions, FWHMs, and separation taken at incoming photon energy of 650 eV. Separation 1 describes the difference between peaks 1 and 2. Separation 2 describes the difference between peaks 2 and 3. All values are in eV. The baseline resolution of energies is 0.05 eV

	Manipulator	**In Cell**	**Precursor Dosing**
FWHM	1.1	1.2	1.3
Lorentz/Gauss ratio	0.2	0.2	0.1
Peak 1 (lattice O 1s)	529.9	530.0	530.0
Peak 2 (C=O, COO^-)	530.9 ± 0.3	531.5 ± 0.3	531.2 ± 0.3
Peak 3 (-OH)	531.8 ± 0.4	532.3 ± 0.4	532.3 ± 0.4
Separation 1	0.9 ± 0.3	1.5 ± 0.3	1.2 ± 0.3
Separation 2	1.0 ± 0.4	0.8 ± 0.3	1.1 ± 0.3

In Table 4.2, we can see that the peak 2 and peak 3 positions change noticeably. This could indicate a change in the chemical environments in the three cases. In Schnadt et al. (*23*), the lattice oxygen peak is kept at 530.05 eV which matches with the lattice peak measured at 530.0 eV in Table 4.2. The separations between the OH peak and C=O peak in O1s spectra for isonicotine and similar molecules range from 1.02 eV to 1.23 eV. In Table 4.2, The separation between Peak 2 and 3 for all cases is close. The separation during the pulsing of precursors, 1.1 eV, matches exactly with nicotinic acid. It is also clear that the peak positions for Peak 2 and Peak 3 differ significantly from each other in the three cases. In the analysis chamber, deposition can only occur due to residual gasses. This could also include the deposition of other impurities that weren't fitted like water. For spectra taken in the cell, Peak 3 matches peak positions during precursor dosing but Peak 2 is shifted. This could indicate that the products

deposited are probably similar to the precursors but the influence of other impurities and chemical shifts not included in the model are significant. The large uncertainties in the peak positions further imply that there are multiple components not included in the shifts. In literature, additional peaks have been assigned by Zhang et al. (*25*), for XPS of TPA deposited on rutile TiO_2(110).

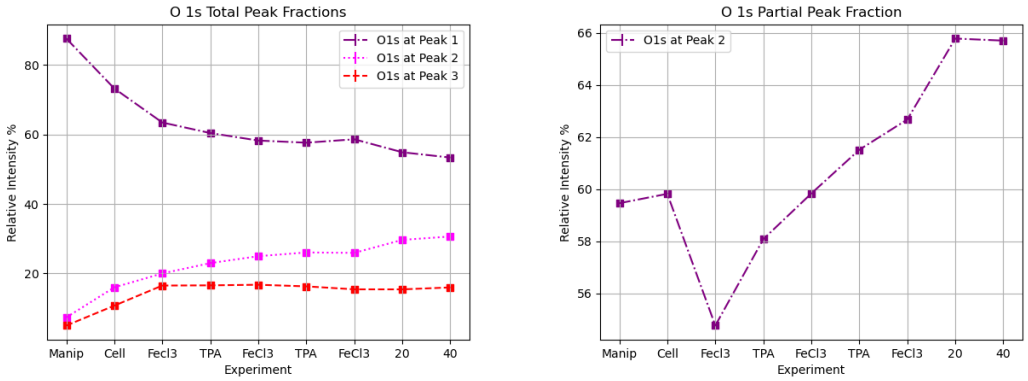

(a) Each peak intensity taken over total intensity (b) 2nd peak over the sum of 2nd and 3rd peak

Figure 4.2: Oxygen peak fractions calculated from spectra in Fig. 4.1

To further understand the processes occurring throughout the experiment, total peak fractions and partial peak fractions are calculated for all O 1s spectra and plotted in Fig. 4.2b. In partial peak fraction for O1s, only Peaks 2 and 3 are considered, while Peak 1 is completely ignored. In Fig. 4.2a, we can see that the O 1s lattice peak fraction reduces from a total of 87.6 % to 53.36 %. This shows a 39 % decrease in the lattice peak's total peak coverage. Peak 2's total peak increases much faster than peak 3. This is reflected in partial peak fractions, with peak 2's partial peak fraction steadily increasing from a minimum of 54.71 % to 65.71 %. This indicates the successful deposition of TPA precursors. This probably stops by twenty MLD cycles because the total peak fractions do not change much between 20 and 40 cycles of MLD.

Protonated carboxylic acids show a one-to-one peak ratio for peaks 2 and 3 corresponding to the two different oxygen atoms. However, from O 1s spectra observed in Fig. 4.1 and O 1s peak fractions in Fig. 4.2, it is clear that this is not the case. The higher intensity in the second peak is due to the contribution of oxygen atoms in deprotonated carboxylic groups. The deprotonated carboxylic group could indicate the formation of Fe-TP MOFs. It is also possible that there are a few deprotonated TPA molecules on the surface of the sample with all the available hydrogen stripped away by chlorine. Fig. 4.3 shows different possible configurations of the deprotonated TPA.

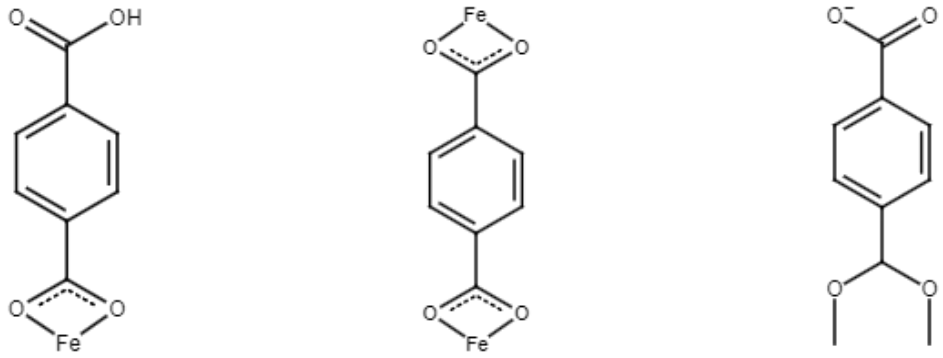

(a) Semi Protonated TPA at the top of Fe-TP layers

(b) Completely deprotonated TPA in Fe-TP layers

(c) Deprotonated TPA attached to a surface

Figure 4.3: Different configurations contributing to the deprotonated carboxylic peak

Following the model used for fitting, Peak 3 is only due to protonated carboxylic acid. Peak 2 is due to both protonated and deprotonated carboxylic acid. The deprotonated carboxylic acid ligand has twice the contribution to Peak 2 due to two similar oxygens. Hence intensity contribution of deprotonated carboxylic ligands is obtained by subtracting Peak 3 from Peak 2 and halving the result. This is described in the equation:

$$I(Deprotonated) = \frac{A(Peak2) - A(Peak3)}{2}, \tag{4.1}$$

where $I(Deporonated)$ is the intensity contribution of deprotonated carboxylic groups, $A(Peak)$ is the area under a given peak. Then the fraction of carboxylic ligands that are deprotonated to the total intensity contribution of all carboxylic oxygen atoms, f_d, is given by

$$f_d = \frac{I(Deprotonated)}{A(Peak2)} \cdot 100. \tag{4.2}$$

The amount of Deprotonated carboxylic ligands calculated are plotted in Fig. 4.4

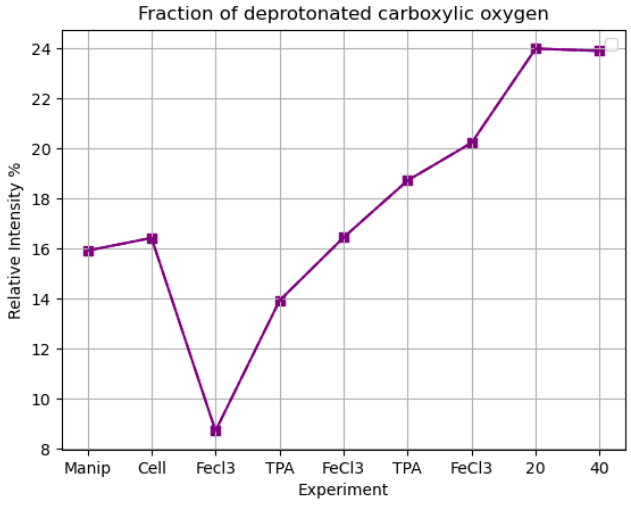

Figure 4.4: Fraction of Deprotonated Carboxylic taken from O 1s spectra.

There is a steady increase of deprotonated TPA from the first half cycle. By the end of 40 cycles, 24 % of the carboxylic ligands measured are deprotonated.

4.2 C 1s

In Fig 4.1, the C 1s spectra show three component peaks at 284.9 eV, 286.9 eV, and 289.1 eV. The benzene ring of the TPA molecule has multiple C-C bonds as can be seen in Fig. 2.2a. This is the source for the 284.9 eV peak. The peak at 289.1 eV corresponds to the binding energy of 1s orbital of the carbon atom in the carboxylic group. C 1s reference spectra measured by Tanskanen et al. (*15*) also show peaks at around the same energies. But no reference shows the middle peak, implying that it is likely a contamination.

The C 1s spectra were also first fitted separately. Since the resulting peak positions and widths did not differ significantly between the experiments. I then held C-C peak position and carboxylic acid peak and fit all C 1s spectra globally with the positions and widths linked in Igor Pro 8 except for the spectrum taken with the sample on the manipulator in the analysis chamber. Since this spectrum was not calibrated, I fit this spectrum separately. As seen in C 1s spectra in Fig. 4.1 this method did not give a very good fit but I continued with it since other elements spectra were all fit based on components. The resulting peak positions are described in Table 4.3. The uncertainties are calculated similarly to O 1s spectra.

Table 4.3: C 1s peak positions, FWHMs, and separation taken at incoming photon energy of 400 eV. Shift 1 describes the difference between peaks 1 and 2. Shift 2 describes the difference between peaks 1 and 3. All values are in eV. The baseline resolution of energies is 0.05 eV

	Manipulator	**In Cell and Dosing**
FWHM	1.8	1.7
Lorentz/Gauss ratio	0.12	0.01
Peak 1 (C-C)	285.5	284.9
Peak 2 (Unknown)	287.1 ± 0.1	286.9 ± 0.1
Peak 3 (C=0)	289.0 ± 0.2	289.1 ± 0.2
Shift 1	1.6 ± 0.1	2.0 ± 0.1
Shift 2	3.5 ± 0.2	4.2 ± 0.2

From Table 4.3, only the chemical shifts of C 1s energy in the manipulator can be compared. The carbon peaks observed in the manipulator are observed due to the deposition of TPA onto the surface of rutile TiO_2(110). The observed chemical shift of the carboxylic carbon peak at 3.5 eV is in line with the chemical shift observed in the literature. Zhang et al (*25*) presented XPS measurements of TPA deposition on rutile TiO_2(110). They measured the chemical shift between the C-C peak and C=O peak to be at 3.8 eV. Schnadt et al. (*23*) presented peak separation ranging from 3.2 to 3.8 eV for C 1s XP spectra of isonicotinic acid. Once in the cell, the carbon peak separation resembles the expected chemical shift of 4.3 eV. (*26*) (*27*). The broad FWHM of 1.7 eV possibly covers both protonated and deprotonated carboxylic acids.

The second peak is either likely due to contamination or part of a reaction mechanism not considered in the models. Its chemical shift of 1.6 eV corresponds to that of carbon C-O-C and C-O-R bonds in literature; their shift ranges from 1.3-1.7 eV (*27*). The bond could be due to active sites on the surface formed due to over-sputtering reacting with deposited organic impurities from prior experiments. Additionally, the TPA precursor used is not of high purity with different types of organic molecules. These impurities could result in, for example, alkyl chains bonding with deprotonated TPA forming ketone bonds. These structures are described in Fig. 4.5.

It is also possible that the carbon of deprotonated carboxylic ligands with the oxygen atoms not bonded to any metals as described in Fig. 4.3c also contributes to Peak 2. This could occur due to excess chlorine stripping away all the hydrogen atoms leaving insufficient iron. This would also explain the small oscillating changes in the partial peak fraction due to $FeCl_3$. All the different possible sources for Peak 2 involved are relatively unstable. The second peak is likely a convolution of multiple chemical shifts.

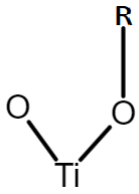

(a) Impurity with a single oxygen bond with the surface

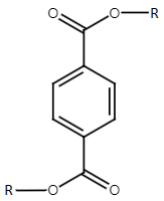

(b) Ketone alkyl bond with TPA

Figure 4.5: Different possible configurations contributing to the deprotonated carboxylic peak

To understand further, I explore peak fractions of the different peaks of C 1s which are plotted in Fig. 4.6. In the analysis chamber, the carboxylic peak has a total peak fraction of 6.6 %. This doubles to 13.3 % in the cell. It reaches a final peak fraction of 10.9 % after 40 cycles of precursor doses. This corresponds well with trends in O 1s peak fractions in Fig. 4.2 for oxygen atoms in the carboxylic groups. They both approximately double as the sample is placed into the cell. Similar to all the O 1s peak fractions, there is no significant difference between 20 and 40 MLD cycles for C 1s peak fractions.

The unknown Peak 2 in C 1s spectra, however, starts with a total peak fraction of 20.0 % and does not change with the sample being moved into the cell. Since this peak does not follow the same trend as O 1s carboxylic peaks it is likely a contamination. But after the sample is moved into the cell, the partial peak fractions of the carboxylic acid and Peak 2 remain mostly constant near 60 %, with slight deviations matching the precursor dosed in. This implies that the peak is also related to the deposition of TPA. Hence, all three possibilities are likely true and Peak 2 is a convolution of all the three sources.

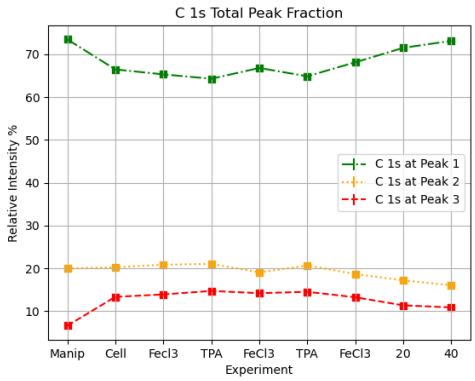

(a) Each peak intensity taken over total intensity

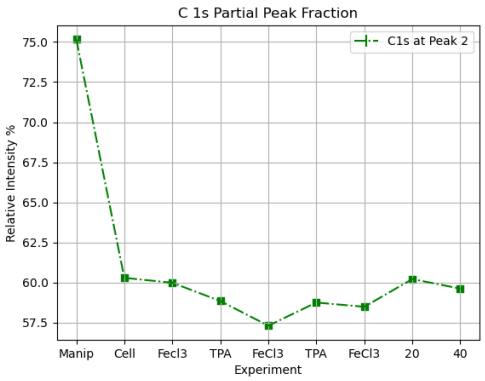

(b) 2nd peak taken over the sum of 2nd and 3rd peak

Figure 4.6: Carbon peak fractions calculated spectra in Fig. 4.1

Getting precise information on the nature of the impurities is difficult without further ex-situ studies of the surface. However, peak ratios can provide some insight. Ideally, for a TPA molecule, the ratio of the C-C peak and carboxylic peak should be 3.0. This comes from six C-C carbons from the benzene ring to the carbon in the two carboxylic ligands from Fig, 2.2a. This ratio is not visible to the large amounts of impurity. Subtracting this ideal contribution from the main C-C peak, a relation between the remaining

impurity C-C bonds and Peak 2 can be investigated. The ratio r is calculated by

$$r = \frac{A(Peak1) - 3A(Peak3)}{A(Peak2)}, \tag{4.3}$$

where $A(Peak)$ is the area under a given peak. The ratio of these two impurity peaks is plotted in Fig. 4.7.

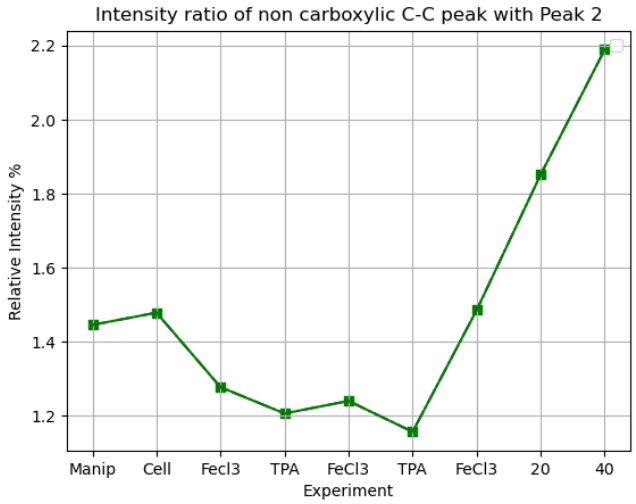

Figure 4.7: Ratio of the intensity of the C-C peak not part of TPA molecules against Peak 2

In Fig. 4.7, the ratio remains constant at around 1.45 before precursors are dosed in. For the first two cycles, this ratio gets lower and is roughly constant around 1.2. The contamination likely dominates and is not covered before dosing precursors. The drop in ratio probably occurs due to the breaking up of the ligands in the contamination and further deposition of a few deprotonated TPA along with impurities dosed in with TPA. The ratio rises again and this could be possible due to more alkyl groups being broken out of impurities but sticking to the surface or just C-C bonds from impurities that are dosed with the low-quality TPA.

The contribution to this peak due to the original contamination likely reduces once the sample is moved into the cell. The oscillation can be explained by both the other types of contributions. However, even after the deposition of TPA slows down between 20 and 40 peaks, there is a steady increase in the C-C bonds on the surface. These are more likely due to the impurities dosed alongside TPA.

4.3 Cl 2p

A 2p orbital undergoes spin-orbit splitting $j = l \pm s = 1/2$, and $3/2$, with a ratio of their areas being 1:2, The Cl 2p spectra in Fig. 4.1 reflect this with two peaks at 198.7 eV and 200.3 eV. Using the wider scan spectroscopy it is clear that trace amounts of chlorine are being deposited onto the surface of the manipulator. Based on how the fitting process went for O 1s and C 1s, Cl 2p spectra collected after precursors were cycled globally with peaks and FWHMs linked in Igor Pro 8. Cl 2p spectra collected in the cell and the manipulator are fitted separately due to different peak positions. Additionally, the wide scan spectroscopy taken in the manipulator was not calibrated. The chemical shift obtained from the global fit was held constant and used in the fitting process for the remaining Cl 2p spectra. The peak positions, widths, and shifts measured are represented in Table 4.4.

Table 4.4: Cl 2p peak positions, FWHMs, and separation taken at an incoming photon energy of 400 eV. Separation describes the difference between peaks 1 and 2. 0.05 eV is the energy uncertainty

	Manipulator	**In Cell**	**Precursor Dosing**
FWHM	1.8	1.7	1.7
Lorentz/Gauss ratio	0.12	0.01	0.01
Peak 1 ($2p_{\frac{3}{2}}$)	285.4	199.1	198.7
Peak 2 ($2p_{\frac{1}{2}}$)	287.0	200.7	200.3
Separation	1.6	1.6	1.6

The peak position of Cl 2p shifts by 0.4 eV with the start of precursor dosing. 2p 3/2 level of Inorganic chlorine ions are lower than organic chlorine and are around 198.5 eV (*28*). Organic chlorine in a covalent bond with sp2 or sp*s* carbon has binding energy at 200 eV (*28*, *29*). With the wide FWHM of the peak, there is likely a contribution from trace amounts of Chlorine bound to carbon atoms. This is especially possible if the unknown C 1s peak is an impurity without a carboxylic group. If this is the case then, the shift makes sense, as more $FeCl_3$ is dosed in, the organic contribution would reduce. Additionally, chlorine should be flushed out in the form of HCl. The presence of chlorine then indicates that either it is binding with titanium or the $FeCl_3$ precursor is physically sticking to the surface. It is also possibly reacting with other impurities and sticking to the layers. This further indicates that a crystalline film is not being developed. Since the data is not normalized, it is difficult to ascertain the changes in intensities. If the intensity was being reduced, it would be more clear whether the chlorine is bonding with titanium. Additionally, a small peak is observed in the chlorine spectra. This is likely due to the Auger decay of argon,

4.4 Ti 2p and Fe 2p

Ti 2p and Fe 2p cannot be simply fitted as they transition metals with multiple oxidation states. However, since the lattice oxidation state dominates, some peak fitting can be done. Hence, only the larger peak corresponding to $2p_{3/2}$ is fitted. The fitted peak position is at 458.6 eV. Lattice titanium is usually in the oxidation state of Ti^{4+}. The asymmetry in $2p_{3/2}$ is indicative of some titanium in the oxidation state of Ti^{3+}. The presence of a lower oxidation state is also indicative of titanium bonds with either chlorine or the impurity. It is difficult to ascertain further. The surface is getting covered with MLD cycles as lattice oxygen's peak fraction gets lower. Though titanium intensities cannot be compared, it does reduce with MLD cycles.

The Fe 2p spectra cannot be fitted further either as the measured Fe2p spectra in Fig. 4.1 do not show the complete spin-orbit splitting. Only Fe $2p_{3/2}$ is visible. There are two oxidation states of iron, Fe^{3+} and Fe^{2+} with a contribution of similar magnitude. The Fe^{2+} is at 709 eV and Fe^{3+} is at 711 eV from literature (*30*). These are shown more clearly in Fig. 4.8. It is important to note stress that the spectra are not normalized. But the lines indicate changes in the intensities at these two points about each other.

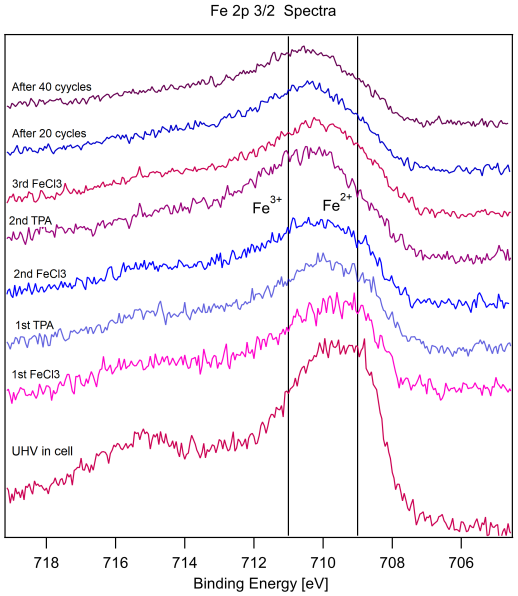

Figure 4.8: All Fe 2p spectra stacked on top along the lines of the two oxidation states of iron

In Fig 4.8, the shoulders for Fe^{3+} over Fe^{2+} slightly oscillate with the pulsing of different precursors. The ratio of the intensity of Fe^{3+} over Fe^{2+} is calculated and shown in Fig. 4.9. It can be seen from this figure, that initially there were more of Fe^{2+} in the cell starting with 0.8. Once the dosing starts Fe^{3+} takes over and stays that way stabilising to the ratio of 1.5 by the end of the experiment. Tanskanen et al. (*15*) explain the larger presence of trivalent iron was indicative of the presence of MOF structures defined in Fig. 2.3.

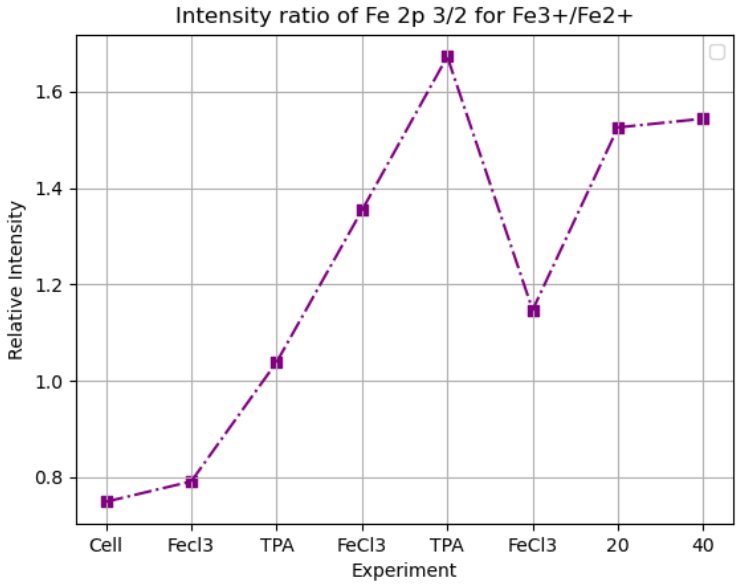

Figure 4.9: Ratio of the intensities of the two oxidation states.

5 Discussion

From spectra taken in the manipulator and the cell in Fig. 4.1, deposition of elements corresponding to both the precursors occurred before they were pulsed in. This indicates that instead of MLD, the different precursors were interacting with each other in the vapor phase leading to CVD. It also implies that these precursors and other residual gasses from previous experiments may have evaporated off the cell walls. From the C 1s spectra, the sample also likely contains contamination. Given that there are multiple possible impurities and residual gasses along with different possible reactions due to CVD, it is difficult to get a clear overview of what is exactly occurring on the surface but some educated guesses can be made. Impurities from residual gasses in the analysis chamber were deposited on the surface of the sample from the beginning of the experiment. Although faint, the presence of iron and chlorine can be seen. The peak contribution of impurity in Fig. 4.5a is also observed.

After the sample was moved into the cell, precursors evaporated from the cell wall and were deposited on the surface. It is likely that deprotonated TPA molecules on the surface with the structure shown in Fig. 4.3c were deposited. This is reflected by the intensity of Fe^{3+} being quite low in comparison to Fe^{2+} but the fraction of deprotonated carboxylic oxygen is about 16 % as shown in Fig. 4.4. This can be further inferred by the fact that the C 1s peak fraction for the second Peak 2 in C 1s spectra remains constant even though there is a significant increase in the total peak fraction of the carboxylic ligands. There was also probably some Fe-TP complex in the vapor phase formed but it is unlikely and difficult to confirm. Organic chlorine is more prevalent in the cell and hence is possibly bonded to alkyl groups in the contamination or the deprotonated TPA. A rough schematic of the surface is drawn in Fig. 5.1.

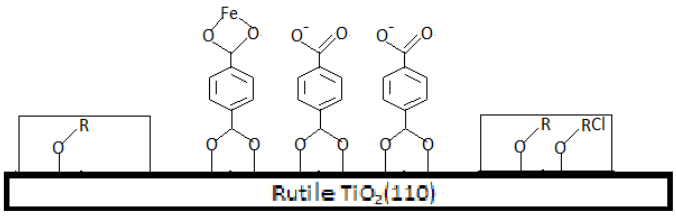

Figure 5.1: Blocks of impurity and layers of deprotonated TPA on the surface with the sample in the cell. Other gasses and impurities possibly in between the surface not drawn.

During the first half cycle with $FeCl_3$, Fe^{3+} shoulder noticeably increases in Fig. 4.8. The amount of deprotonated carboxylic ligands measured in O 1s drops by half down to 8%. This indicates that even though only $FeCl_3$ was pulsed in, more of the TPA was being deposited on the surface. Some of the pulsed in $FeCl_3$ likely formed Fe-TP complexes with the highly reactive standing deprotonated TPA on the surface. The contamination on the surface was not getting covered as the C-O peak in spectra continued to maintain its peak fraction Some of the residue products coming off of the walls could also be the same as the contamination on the sample.

At some point by 20 cycles or earlier, deposition of TPA stopped or was greatly reduced. Instead,

only the alkyl impurities dosed in with the poor-quality TPA were deposited. This is reflected by the increased peak fractions of C-C bonds in Fig. 4.7 and Fig. 4.6a, while all other peak ratios and fractions remain constant or decrease. The fraction of deprotonated carboxylic ligands from the O 1s spectra was 24 % at the end of the 40 cycles. Given, that there were still TPA molecules and $FeCl_3$ in the call and surface in higher proportions, it is unlikely that any of the deprotonated carboxylic ligands in the highly reactive state in Fig. 4.3c would remain. Then it is reasonable to assume that the source of the deprotonated carboxylic acid is entirely due to the Fe-TP complexes. Hence at the end of 40 cycles, 24 % of the TPA deposited on the surface form Fe-TP MOFs. Additionally, The presence of the peak at 286.9 eV at the end of the 40 cycles suggests that the contamination was not covered and the presence of inorganic chlorine throughout the experiment shows that the Fe-TP MOF grown is amorphous. A visual representation of the surface is shown in Fig. 5.2.

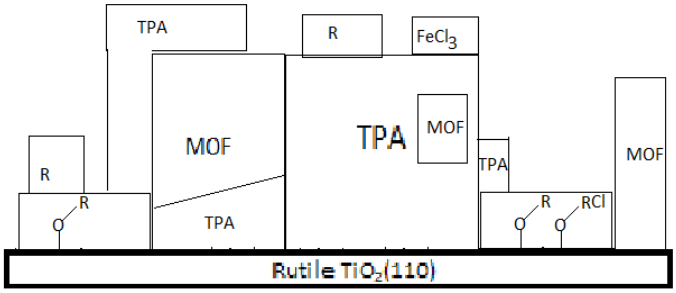

Figure 5.2: This image is an approximate representation based on the educated guesses from XPS. MOF blocks are not uniform but amorphous MOF structures with chlorine and other impurities trapped within. The MOF structures would grow on top of the deprotonated TPA and are likely sporadically spread out. Most of the carboxylic ligands are due to TPA, represented by a larger quantity of TPA blocks. Blocks with R represent Layers of only alkyl impurities being adsorbed on the surface after deposition of TPA slows down. TPA blocks also encompass different possible TP configurations.

6 Conclusion

Taking account of everything presented, it is clear that a crystalline Fe-TP film did not grow on the surface. At least for the first few cycles, CVD occurred instead of ALD due to residual gasses and contamination. The precursors and other products from the previous experiments during the same beamtime had condensed onto the walls of the ALD reactor cell and thus contributed to residual gasses and CVD. Since the experiment presented was done toward the end of the beamtime, there is a higher likelihood of build-up of the precursors on the cell walls. The sample was also used in another experiment in the meantime which likely contributed to the contamination.

The contamination, reaction products, and residual gasses prevented further growth of crystalline ultrathin MOF films with additional cycles. Consequently, models then used to describe and fit the processes occurring at the surface are not representative of everything occurring on the sample. Hence, peak ratios and peak fractions of all the other elements recorded had to be taken into consideration to make educated estimates. Based on Sec. 4.1, even with an optimistic assumption that all deprotonated carboxylic ligands at the end of 40 cycles are part Fe-TP MOFs, only 24 % of the measured TPA on the surface formed MOFs. The MOFs produced likely were amorphous and did not cover contaminated regions of the rutile $TiO_2(110)$ surface. The growth of these MOFs occurred gradually with more cycles of MLD but the deposition of TPA and other related impurities was more common. The depositions of TPA completely stop or are drastically reduced by the end of 20 cycles of MLD. This is most likely due to the contamination and amorphous structure and the temperatures and pressure of precursors used are not optimised.

Growth of crystalline MOF films with transition metals is generally more difficult due to the directional bonding of these metals. Tanskanen et al. (*15*) did grow crystalline films with $FeCl_3$ but the information on the preparation of these films is not quite clear. Since some Fe-TP MOFs likely did grow despite impurities and complications due to CVD, crystalline ultrathin films of Fe-TP MOFs could be achieved. Further ex-situ studies, like Scanning Tunnel Microscopy (STM), need to be conducted to properly quantify and evaluate the structure of the surface. This can allow for better tuning of the parameters needed to develop methods to grow ultrathin Fe-TP films reliably.

References

(*1*) Li, H., Eddaoudi, M., O'Keeffe, M. **and** Yaghi, O. M. (1999). Design and synthesis of an exceptionally stable and highly porous metal-organic framework. *Nature 402*, 276–279.

(*2*) Cheng, M., Lai, C., Liu, Y., Zeng, G., Huang, D., Zhang, C., Qin, L., Hu, L., Zhou, C. **and** Xiong, W. (2018). Metal-organic frameworks for highly efficient heterogeneous Fenton-like catalysis. *Coordination Chemistry Reviews 368*, 80–92.

(*3*) Felix Sahayaraj, A., Joy Prabu, H., Maniraj, J., Kannan, M., Bharathi, M., Diwahar, P. **and** Salamon, J. (2023). Metal–Organic Frameworks (MOFs): The Next Generation of Materials for Catalysis, Gas Storage, and Separation. *Journal of Inorganic and Organometallic Polymers and Materials 33*, 1757–1781.

(*4*) Baumann, A. E., Burns, D. A., Liu, B. **and** Thoi, V. S. (2019). Metal-organic framework functionalization and design strategies for advanced electrochemical energy storage devices. *2*, 1–14.

(*5*) Chernikova, V., Yassine, O., Shekhah, O., Eddaoudi, M. **and** Salama, K. N. (2018). Highly sensitive and selective SO2 MOF sensor: the integration of MFM-300 MOF as a sensitive layer on a capacitive interdigitated electrode. *Journal of Materials Chemistry A 6*, 5550–5554.

(*6*) Moosavi, S. M., Nandy, A., Jablonka, K. M., Ongari, D., Janet, J. P., Boyd, P. G., Lee, Y., Smit, B. **and** Kulik, H. J. (2020). Understanding the diversity of the metal-organic framework ecosystem. *Nature Communications 11*, 4068.

(*7*) Moghadam, P. Z., Li, A., Wiggin, S. B., Tao, A., Maloney, A. G. P., Wood, P. A., Ward, S. C. **and** Fairen-Jimenez, D. (2017). Development of a Cambridge Structural Database Subset: A Collection of Metal–Organic Frameworks for Past, Present, and Future. *Chemistry of Materials 29*, 2618–2625.

(*8*) Li, J., Yu, C., Wu, Y.-n., Zhu, Y., Xu, J., Wang, Y., Wang, H., Guo, M. **and** Li, F. (2019). Novel sensing platform based on gold nanoparticle-aptamer and Fe-metal-organic framework for multiple antibiotic detection and signal amplification. *Environment International 125*, 135–141.

(*9*) Zhi, K., Xu, J., Li, S., Luo, L., Liu, D., Li, Z., Guo, L. **and** Hou, J. (2024). Progress in the Elimination of Organic Contaminants in Wastewater by Activation Persulfate over Iron-Based Metal–Organic Frameworks. *Nanomaterials 14*, 473.

(*10*) Ren, J. **and** Jen, T.-C. (2021). Atomic layer deposition (ALD) assisting the visibility of metal-organic frameworks (MOFs) technologies. *Coordination Chemistry Reviews 430*, 213734.

(*11*) D'Acunto, G. Reaction Mechanisms and Dynamics in the Early Stage of High-$\varkappa$ Oxide Atomic Layer Deposition : Investigations by *In Situ* and *Operando* X-ray Photoemission Spectroscopy, thesis/doccomp, Lund University, 2022.

(*12*) D'Acunto, G., Troian, A., Kokkonen, E., Rehman, F., Liu, Y.-P., Yngman, S., Yong, Z., McKibbin, S. R., Gallo, T., Lind, E., Schnadt, J. **and** Timm, R. (2020). Atomic Layer Deposition of Hafnium Oxide on InAs: Insight from Time-Resolved in Situ Studies. *ACS Applied Electronic Materials 2*.

(*13*) D'Acunto, G., Shayesteh, P., Kokkonen, E., Boix de la Cruz, V., Rehman, F., Mosahebfard, Z., Lind, E., Schnadt, J. **and** Timm, R. (2023). Time evolution of surface species during the ALD of high-k oxide on InAs. *Surfaces and Interfaces 39*, 102927.

(*14*) Lee, S., Baek, G., Lee, J.-H., Van, T. T. N., Ansari, A. S., Shong, B. **and** Park, J.-S. (2020). Molecular layer deposition of indicone and organic-inorganic hybrid thin films as flexible transparent conductor. *Applied Surface Science 525*, 146383.

(*15*) Tanskanen, A. **and** Karppinen, M. (2018). Iron-Terephthalate Coordination Network Thin Films Through In-Situ Atomic/Molecular Layer Deposition. *Scientific Reports 8*, 8976.

(*16*) Chui, S. S.-Y., Lo, S. M.-F., Charmant, J. P. H., Orpen, A. G. **and** Williams, I. D. (1999). A Chemically Functionalizable Nanoporous Material [Cu3(TMA)2(H2O)3]n. *Science 283*, 1148–1150.

(*17*) Ma, M., Bétard, A., Weber, I., Al-Hokbany, N. S., Fischer, R. A. **and** Metzler-Nolte, N. (2013). Iron-Based Metal–Organic Frameworks MIL-88B and NH2-MIL-88B: High Quality Microwave Synthesis and Solvent-Induced Lattice "Breathing". *Crystal Growth & Design 13*, 2286–2291.

(*18*) Millange, F., Serre, C. **and** Férey, G. (2002). Synthesis, structure determination and properties of MIL-53as and MIL-53ht. *Chemical Communications*, 822–823.

(*19*) Leus, K., Dendooven, J., Tahir, N., Ramachandran, R. K., Meledina, M., Turner, S., Van Tendeloo, G., Goeman, J. L., Van der Eycken, J., Detavernier, C. **and** Van Der Voort, P. (2016). Atomic Layer Deposition of Pt Nanoparticles within the Cages of MIL-101: A Mild and Recyclable Hydrogenation Catalyst. *Nanomaterials 6*, 45.

(*20*) Hüfner, S., *Photoelectron Spectroscopy*; Advanced Texts in Physics; Springer: Berlin, Heidelberg, 2003.

(*21*) Kokkonen, E., Kaipio, M., Nieminen, H.-E., Rehman, F., Miikkulainen, V., Putkonen, M., Ritala, M., Huotari, S., Schnadt, J. **and** Urpelainen, S. (2022). Ambient pressure x-ray photoelectron spectroscopy setup for synchrotron-based in situ and operando atomic layer deposition research. *Review Of Scientific Instruments 93*, 013905.

(*22*) Major, G. H., Fairley, N., Sherwood, P. M. A., Linford, M. R., Terry, J., Fernandez, V. **and** Artyushkova, K. (2020). Practical guide for curve fitting in x-ray photoelectron spectroscopy. *Journal of Vacuum Science & Technology A 38*, 061203.

(*23*) Schnadt, J., O'Shea, J. N., Patthey, L., Schiessling, J., Krempaský, J., Shi, M., Mårtensson, N. **and** Brühwiler, P. A. (2003). Structural study of adsorption of isonicotinic acid and related molecules on rutile TiO2(1 1 0) II: XPS. *Surface Science 544*, 74–86.

(*24*) Patthey, L., Rensmo, H., Persson, P., Westermark, K., Vayssieres, L., Stashans, A., Petersson, Å., Brühwiler, P. A., Siegbahn, H., Lunell, S. **and** Mårtensson, N. (1999). Adsorption of bi-isonicotinic acid on rutile TiO2(110). *The Journal of Chemical Physics 110*, 5913–5918.

(*25*) Zhang, W., Cao, L., Wan, L., Liu, L. **and** Xu, F. (2013). A Photoelectron Spectroscopy Study on the Interfacial Chemistry and Electronic Structure of Terephthalic Acid Adsorption on TiO2(110)-(1×1) Surface. *The Journal of Physical Chemistry C 117*, 21351–21358.

(*26*) Moore, R. G. C., Evans, S. D., Shen, T. **and** Hodson, C. E. C. (2001). Room-temperature single-electron tunnelling in surfactant stabilised iron oxide nanopjournals. *Physica E: Low-dimensional Systems and Nanostructures 9*, 253–261.

(*27*) Grey, L. H., Nie, H.-Y. **and** Biesinger, M. C. (2024). Defining the nature of adventitious carbon and improving its merit as a charge correction reference for XPS. *Applied Surface Science 653*, 159319.

(*28*) Chastain, J. **and** King Jr, R. C. (1992). Handbook of X-ray photoelectron spectroscopy. *Perkin-Elmer Corporation 40*, 221.

(*29*) Papirer, E., Lacroix, R., Donnet, J.-B., Nansé, G. **and** Fioux, P. (1995). XPS study of the halogenation of carbon black—Part 2. Chlorination. *Carbon 33*, 63–72.

(*30*) Yamashita, T. **and** Hayes, P. (2008). Analysis of XPS spectra of Fe2+ and Fe3+ ions in oxide materials. *Applied Surface Science 254*, 2441–2449.